



**HAL**  
open science

## Evidence for a build-in remnant field in symmetrically contacted MAPbB<sub>3</sub> X-ray detectors

Ferdinand Ledee, Javier-Alejandro Mayen Guillen, Stephanie Lombard, Julien Zaccaro, Jean-Marie Verilhac, Eric Gros d'Aillon

### ► To cite this version:

Ferdinand Ledee, Javier-Alejandro Mayen Guillen, Stephanie Lombard, Julien Zaccaro, Jean-Marie Verilhac, et al.. Evidence for a build-in remnant field in symmetrically contacted MAPbB<sub>3</sub> X-ray detectors. *Journal of Applied Physics*, 2023, 134, pp.195703. 10.1063/5.0170580 . cea-04468082

**HAL Id: cea-04468082**

**<https://cea.hal.science/cea-04468082>**

Submitted on 20 Feb 2024

**HAL** is a multi-disciplinary open access archive for the deposit and dissemination of scientific research documents, whether they are published or not. The documents may come from teaching and research institutions in France or abroad, or from public or private research centers.

L'archive ouverte pluridisciplinaire **HAL**, est destinée au dépôt et à la diffusion de documents scientifiques de niveau recherche, publiés ou non, émanant des établissements d'enseignement et de recherche français ou étrangers, des laboratoires publics ou privés.

# Evidence for a build-in remnant field in symmetrically contacted MAPbBr<sub>3</sub> X-ray detectors

Ferdinand Lédée<sup>1,2,\*</sup>, Javier Mayén-Guillen<sup>2</sup>, Stéphanie Lombard<sup>2</sup>, Julien Zaccaro<sup>3</sup>, Jean-Marie Verilhac<sup>2</sup>, Eric Gros-Daillon<sup>1,\*</sup>

<sup>1</sup> Grenoble Alpes University, CEA, LETI, DOPT, F38000 Grenoble, France

<sup>2</sup> Grenoble Alpes University, CEA, LITEN, DTNM, F38000 Grenoble, France

<sup>3</sup> Grenoble Alpes University, CNRS, Grenoble INP, Institut Néel, F38042 Grenoble, France

\* [ferdinand.ledée@cea.fr](mailto:ferdinand.ledée@cea.fr) ; [eric.grosdaillon@cea.fr](mailto:eric.grosdaillon@cea.fr)

Keywords: X-ray detectors, halide perovskites, sensitivity, simulation, Hecht equation

## 1. Abstract

Millimeter-thick methylammonium lead tribromide (MAPbBr<sub>3</sub>) single crystal X-ray detectors have recently raised attention due their high X-ray attenuation efficiency and good charge transport properties. However, an intriguing feature of the photocurrent response of MAPbBr<sub>3</sub> detectors has been largely overlooked in the literature. After biasing, transient sensitivity is measured under X-rays at short-circuit (Bias = 0V), thus revealing a large remnant electric field that build-up under bias. Here, we exploit the X-ray sensitivity of MAPbBr<sub>3</sub> detectors at zero-bias in order to probe the internal built-in field, as well as to investigate the charge transport properties of the perovskite material. Our model derived from the Hecht equation is able to fully rationalize the response of the detectors both at short-circuit and under moderate applied bias. Moreover, we provide a method for the estimation of the internal electric field, and for the sum of the electrons and holes mobility-lifetime products  $\mu_e \tau_e + \mu_h \tau_h$ . This general method could extend to any perovskite-based X-ray detector exhibiting transient sensitivity at zero-bias.

## 2. Introduction

Metal halide perovskites are the current key players in the field of radiation detection, challenging the performance of classical semiconductors in several applications while maintaining competitive manufacturing costs. In particular, methylammonium lead tribromide (MAPbBr<sub>3</sub>) in single crystal form is one of the most intensively studied emerging material for the direct detection of X-rays.[1]–[7] Despite the high quality of these as-grown single crystals,[8]–[10] several features of this semiconducting material remain unexplained. Notably, in some cases the photocurrent response of MAPbBr<sub>3</sub> seems to deviate from the Hecht model.[1], [3], [4], [6] Hecht model is the most widely used model to describe the photoresponse of semiconductor-based X-rays detectors such as CdTe, CdZnTe,

37 GaAs; and shall be applied as well to halide perovskites.[11]–[13] In particular for MAPbBr<sub>3</sub>, it is often  
 38 applied in the form displayed in Eq. (2) to fit the experimental sensitivity-voltage (*S-V*) dataplots in  
 39 order to extract the mobility-lifetime product  $\mu\tau$  of the electronic charge carriers.[1], [2], [14], [15] Yet,  
 40 previous work from our group revealed that the X-ray photoresponse of Cr/MAPbBr<sub>3</sub>/Cr devices is not  
 41 in accordance with the Hecht model.[16] Moreover, in the recent work of Alvarez *et al*, it is shown that  
 42 sizeable X-ray photocurrent can be measured in Cr/MAPbBr<sub>3</sub>/Cr devices in short-circuit conditions.  
 43 Unlike photovoltaic-inspired devices that provide stable photocurrent output under irradiation,[17],  
 44 [18] the X-ray photocurrent measured in Cr/MAPbBr<sub>3</sub>/Cr photoconductors at zero-bias decays over  
 45 time and follows the relaxation dynamics of the dark current.[19] We propose that this is the outcome  
 46 of a residual electric field created upon biasing that relaxes when the bias is removed. This residual  
 47 field would originate from the build-up of a space-charge when the Cr/MAPbBr<sub>3</sub>/Cr device is biased,  
 48 and would result in a diminished net applied electric field under operation. The internal electric field  
 49 would be responsible for the anomalies listed above, in particular the discrepancy between the  
 50 experimental sensitivity-voltage (*S-V*) data and the Eq. (2).

51 This paper aims to provide a detailed picture of the X-ray photoresponse of Cr/MAPbBr<sub>3</sub>/Cr single  
 52 crystal devices under short-circuit conditions. Starting from the assumption that the residual electric  
 53 field prevalent at zero-bias is also present under an externally applied bias, we developed a model  
 54 derived from the Hecht model that is able to assess with great precision the internal electric field that  
 55 opposes the externally applied bias under operation. In addition, we use our model to bring an  
 56 alternative pathway to establish relevant intervals for the  $\mu\tau$  products in MAPbBr<sub>3</sub>-based detectors.  
 57 We believe that this work sheds new light on the X-ray photoresponse of MAPbBr<sub>3</sub> detectors; and will  
 58 give new insights into the residual charges that are formed in millimeter-thick lead halide perovskite  
 59 devices under bias, as well as their aftermath on the detection performances.

60

### 61 **3. Discussion on the internal electric field**

62

63 In a semiconductor-based planar detector, the photocurrent measured under X-ray results from the  
 64 induction of current by the photogenerated charges on the contact electrodes, also referred as the  
 65 Ramo-Shockley theorem.[20] The integration of the photocurrent over the X-ray pulse duration brings  
 66 one of the methods that allow to estimate the sensitivity, hereby expressed in  $\mu\text{C mGy}^{-1} \text{cm}^{-2}$ . Without  
 67 any trapping, the sensitivity reaches a maximum value and depends only on the amount of  
 68 photogenerated charges in the semiconductor :

$$69 \quad S_0 = \int s_0(x)dx \quad (1)$$

70 With  $s_0$  the charge generated in an elemental volume  $dx$  of the semiconductor (see Methods section).  
 71 With trapping and for a planar detector with two facing electrodes, the analytical integration of the  
 72 Ramo theorem over the charge carrier lifetime  $\tau$  gives the sensitivity-voltage (*S-V*) relationship which  
 73 reads:

$$74 \quad S(V) = \frac{S_0\mu\tau V}{L^2} \left[ 1 - \exp\left(-\frac{L^2}{\mu\tau V}\right) \right] \quad (2)$$

75 With  $S_0$  the maximum sensitivity,  $\mu$  the charge carrier mobility,  $V$  the applied bias and  $L$  the distance  
 76 between the electrodes. This relation is only valid when the following conditions are met altogether i)  
 77 the energy is absorbed close to the irradiated electrode ; ii) only one type of charge carrier drifts in the

78 device; iii) the electric field is uniform.[11] When the photocurrent contribution from the second  
 79 charge carrier type cannot be neglected, e.g. when the absorption length is not negligible with respect  
 80 to  $L$ , the relation becomes a function of the depth. It translates into the two-carriers Hecht equation  
 81 which reads:

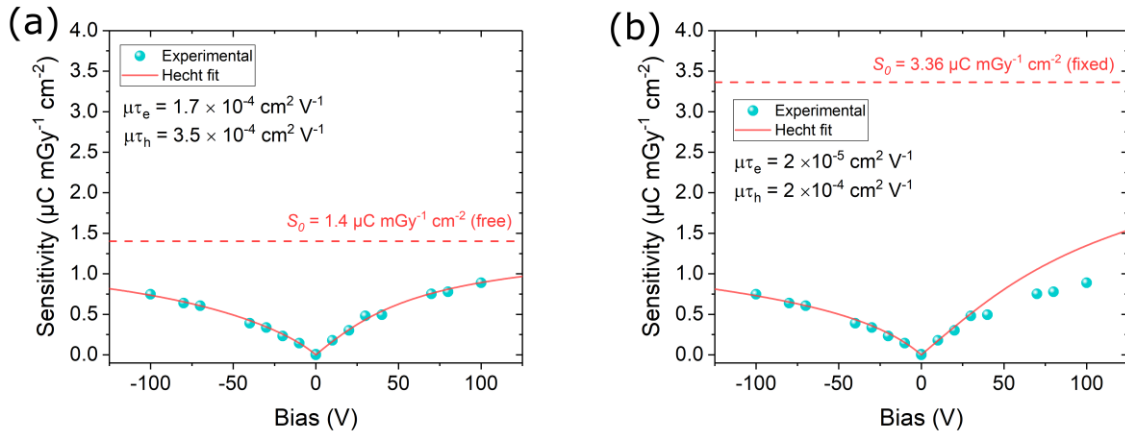
$$82 \quad \eta(x, V) = \frac{\mu_e \tau_e V}{L^2} \left[ 1 - e^{-\frac{xL}{\mu_e \tau_e V}} \right] + \frac{\mu_h \tau_h V}{L^2} \left[ 1 - e^{-\frac{L(L-x)}{\mu_h \tau_h V}} \right] \quad (3)$$

83 Where  $\eta$  is the charge induction efficiency (CIE),  $x$  is the position of creation of the charge carriers  
 84 ( $0 < x < L$ ), and the subscripts e and h denote for electrons and holes, respectively. The  $S$ - $V$  relationship  
 85 now reads :

$$86 \quad S(V) = \int s_0(x) \eta(x, V) dx \quad (4)$$

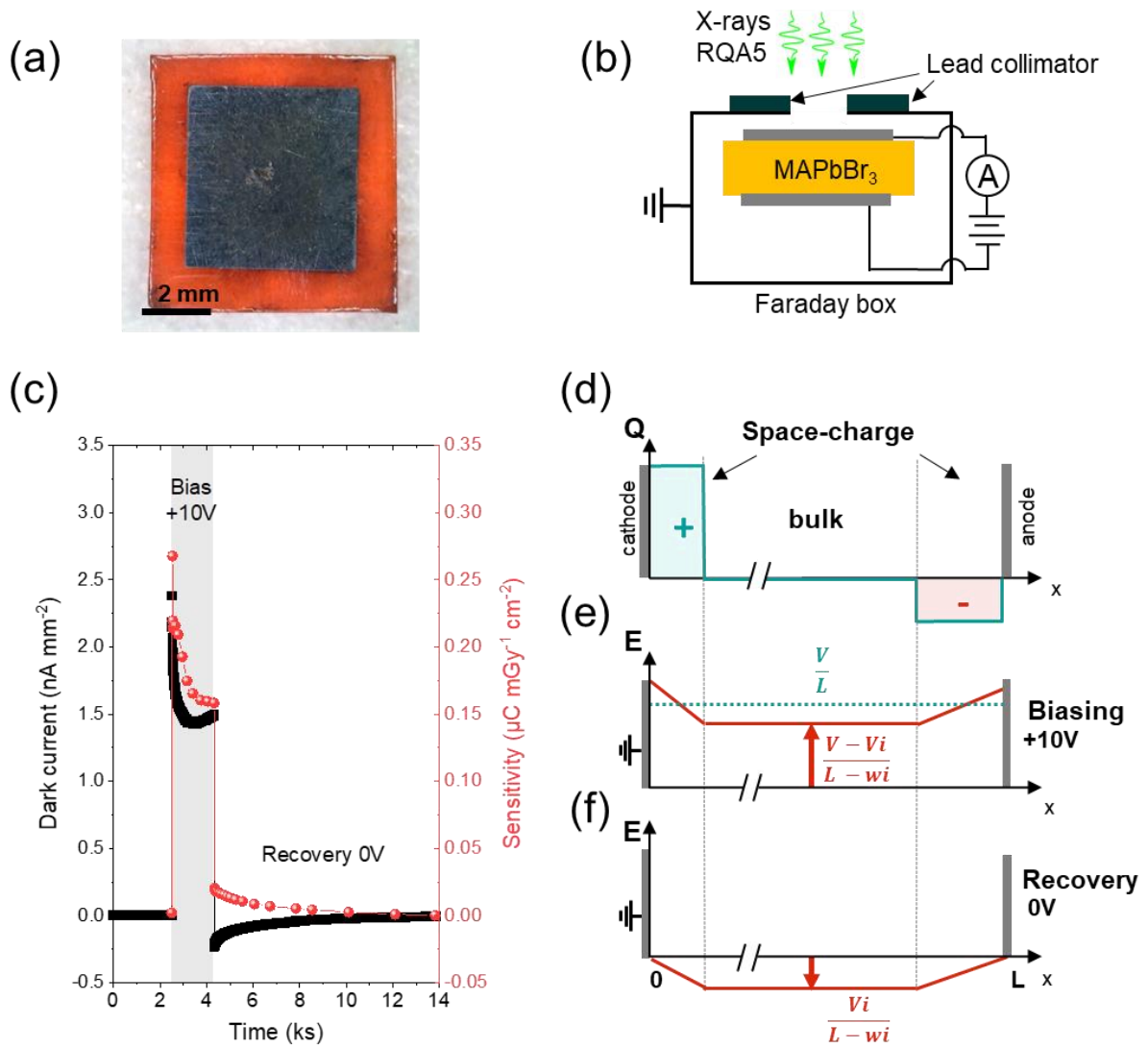
87 With  $s_0$  the charge generated in an elemental volume  $dx$  of the semiconductor (see Methods section).  
 88 Further details on the fabrication of the detector, on the Hecht model and calculation of  $S_0$  are  
 89 provided in the Methods section.

90 A common approach in the research applied to perovskite X-ray detectors consists of using equation  
 91 (2) or (4) to fit the experimental sensitivity-voltage data in order to extract a value for the mobility-  
 92 lifetime product  $\mu\tau$ . In most of the works, the maximum sensitivity  $S_0$  (or the maximum induced  
 93 current  $I_0$ ) is not estimated, and thus is set as a free parameter in the Hecht fits. We propose that this  
 94 produces a lot of misinterpretation of the  $S$ - $V$  data. As an illustration, Fig. 1 displays experimental  $S$ - $V$   
 95 curve for a MAPbBr<sub>3</sub> single crystal planar detector fitted both with and without a calibrated and fixed  
 96  $S_0$  value. The  $\mu\tau$  product for electrons extracted from the fit differs by almost an order of magnitude  
 97 depending on the method. Furthermore, in Figure 1b, the Hecht model is not in good accordance with  
 98 the experimental  $S$ - $V$ . The experimental sensitivity measured at higher biases is lower than the value  
 99 predicted with the Hecht model, and seems to plateau to a much lower value than  $S_0$  (typically  $S_{max} =$   
 100  $0.25 S_0$ ). Here the  $S_0$  value has been estimated using Klein's rule ( $W = 14/5 * E_g + 0.5$ )[21], however  
 101 choosing a  $W$  value equal to that experimentally determined for CsPbBr<sub>3</sub> by He *et al.* does not change  
 102 the result of the fit (see Fig. S1 for further details).[22] Furthermore, the Many equation also fails to fit  
 103 our experimental  $S$ - $V$  data (Fig. S4). This behavior has already been observed by our group for all our  
 104 MAPbBr<sub>3</sub>-based devices, as well as for various perovskite compositions.[16] The plateau of the  
 105 sensitivity to a lower  $S$  value in MAPbBr<sub>3</sub>-based devices is overlooked in the literature because the  
 106 maximum sensitivity  $S_0$  (or  $I_0$ ) is mostly set as a free parameters as in Fig.1a.[1] Note that in that case,  
 107 the  $S_0$  value is not linked to any macroscopic quantity. Besides,  $S$ - $V$  graphs are often plotted in semi-  
 108 log scale, which misleads the reader into thinking that the fit is better than it actually is (see Fig.S2 for  
 109 an illustration). [1], [2], [14] Remarkably, we carried out a  $S$ - $V$  measurement adding a depolarization  
 110 time (bias =0V) inbetween each bias step. Despite the relatively long (5-10 min) depolarization time  
 111 and the relatively short ( $\approx$  5s) bias pulse duration, the low  $S_{max}$  plateau is still present and the Hecht  
 112 equation fails to fit the results (see Fig. S3 for further details). We attribute the plateau at lower  $S_0$   
 113 value to a non-uniform electric field across the detector at higher applied bias. Several phenomena  
 114 may distort the electric field, including charge trapping in the bulk of the semiconducting material [23],  
 115 surface polarization,[24] depletion region due to Schottky contacts [25] or ion accumulation at the  
 116 vicinity of the contact electrodes.[26] All of these potential mechanisms may lead to mis-estimation  
 117 of the values of  $\mu\tau$  products in MAPbBr<sub>3</sub>-based detectors using Eq. 2. To date, the hypothesis of ion  
 118 accumulation seems to be the prevailing one in the literature on perovskite detectors.[26], [27]  
 119 Considering the numerous works on the migration of ionic species in MAPbBr<sub>3</sub>,[28]–[31] it seems to  
 120 be the most possible explanation to the best of our knowledge.



121  
 122 Fig. 1. Sensitivity-voltage plots of a MAPbBr<sub>3</sub> device with corresponding two-carriers Hecht fits with (a)  
 123 S<sub>0</sub> set as a free parameter and (b) S<sub>0</sub> set as the total charge generated in the device. See Methods for  
 124 more details on the calculation of S<sub>0</sub>.

125  
 126 Another intriguing feature of our MAPbBr<sub>3</sub>-based devices arises from the so-called *bias memory effect*  
 127 in short-circuit conditions. As notified in previous works, after biasing, MAPbBr<sub>3</sub> and other halide  
 128 perovskites devices exhibit transient dark current relaxation with inverted sign at 0V.[19], [32] In  
 129 addition the dark current transient is accompanied with non-negligible sensitivity under X-rays during  
 130 the relaxation window at 0V, as shown in Fig.2(c). Notably, the sensitivity at 0V decays over time with  
 131 slow dynamics akin to the dark current transient (Fig.S5). Fig.2(d-e-f) provides a depiction of the *bias*  
 132 *memory effect*. Several works suggest that upon biasing, the displacement of mobile ions toward the  
 133 contact electrodes builds up a space-charge that distorts the electric field (Fig.2d and 2e).[27], [33]  
 134 Consequently the net electric field in the bulk region of the device is reduced with respect to the  
 135 uniform case (dotted blue line in Fig. 2e). [19][27] In the present work, we approximate the electric  
 136 field in the bulk to  $\frac{V-V_i}{L-w_i}$  where V<sub>i</sub> is the potential drop associated to the space-charge formation, w<sub>i</sub>  
 137 the total space-charge width. When the bias is subsequently released, the space-charge built-up by  
 138 the accumulations of ions prevails and creates a residual electric field that we approximate to  $\frac{V_i}{L-w_i}$   
 139 in the bulk region (Fig. 2f). Note that during both biasing and recovery steps, we deem the electric field  
 140 to be flat in the bulk region of the detector and non-uniform in the space-charge regions, in accordance  
 141 with previous works.[19], [26] After bias removal, the residual field during the recovery step gradually  
 142 fades out as the mobile ions return to equilibrium. It should be noted again that the present work does  
 143 not assume an origin for the internal electric field, which can originate from any space charge build-up  
 144 in the perovskite material. Nonetheless, the migration of mobile ions provides a comprehensive  
 145 picture to describe these results, as depicted in the schematics of Fig.2d. In this picture, the dark  
 146 current recovery measured at 0V would originate from an interplay between ionic and electronic  
 147 currents[19]; and the photogenerated charge carriers may drift along the residual electric field at 0V  
 148 during a characteristic recovery time, thus generating decaying photocurrent over time (Fig. 2c).



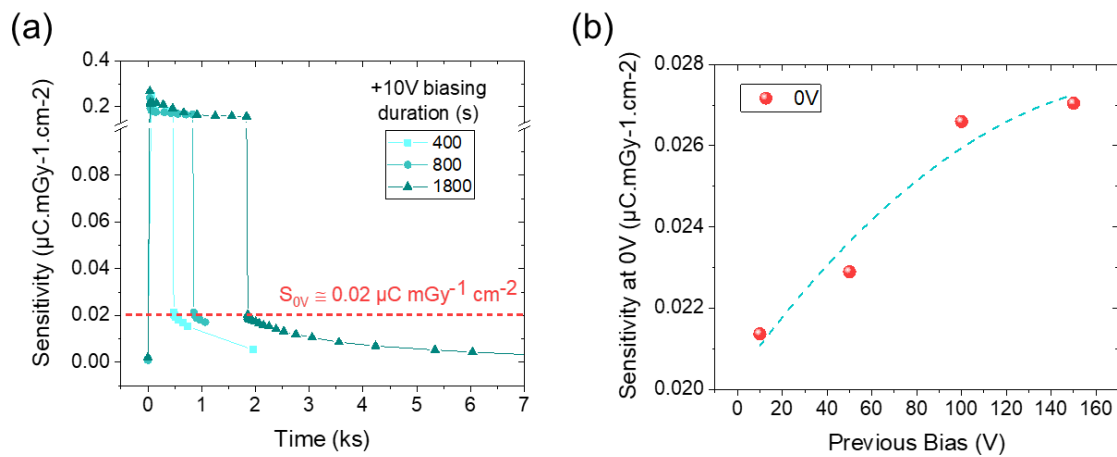
149

150 Fig. 2. (a) Microscope picture of a typical Cr/MAPbBr<sub>3</sub>/Cr single crystal device used in this study. (b)  
 151 Schematic of the X-ray irradiation setup. (c) Dark current (black curve) and sensitivity-time (red curve)  
 152 measurements during both biasing et recovery steps. (d-e-f) Proposed model for the electric field  
 153 profile in the depth of the device during the experiment. The electric field is supposed linear in the  
 154 bulk and is approximated by  $\frac{V-V_i}{L-wi}$  during the biasing step (e), and  $\frac{V_i}{L-wi}$  during the recovery step (f).

155 Fig.3 gives additional insights about the residual electric field for a Cr/MAPbBr<sub>3</sub>/Cr single crystal device.  
 156 For the moderate biasing time range (400-2000 seconds) and applied bias (10V) used in this  
 157 experiment, the sensitivity at 10V decreases slightly over time (Fig.3a). We attribute this to the space-  
 158 charge build-up that gradually reduces the net electric field in the bulk region of the device, with a  
 159 consequent reduction of the sensitivity.[27] When the bias is released, sensitivity is measured at 0V  
 160 owing to the residual electric field. Notably, the sensitivity measured at 0V immediately after removing  
 161 the bias is the same regardless of the biasing duration in the [400-1800s] bias duration range  
 162 investigated in this work (Fig.3a). It suggests that, for this 2-mm thick MAPbBr<sub>3</sub> device, the space-  
 163 charge build-up is rather fast ( $\leq 400$  seconds) and remains constant. Thus, the sensitivity of the device  
 164 at 0V is initially the same for biasing duration  $\geq 400$ s. In addition, the residual electric field varies with  
 165 the applied bias. As seen in Fig 3b, the sensitivity at 0V measured immediately after removing the bias  
 166 scales with the previous bias value accordingly, indicating that the space-charge build-up is a function  
 167 of the applied electric field; that could indicate the drifting of mobile ionic species.[30], [31] However,

168 we noted only a 30% increase in the residual sensitivity at 0V with bias increasing from 10V to 150V,  
 169 which would suggest that most of the mobile ions have already reach the electrode for biases  $\geq 10V$   
 170 and biasing duration  $\geq 400$  seconds. Markedly, this experiment could partially explain why the  
 171 experimental S-V is not well fitted with the Hecht equation in Fig.1b. Along with the rising space-charge  
 172 that produces distortion of the electric field at high bias, the net electric field in the bulk is progressively  
 173 reduced by the internal field build-up as the applied bias is increased. As a consequence, the net  
 174 electric field in the device can be underestimated, as it will be discussed below. Finally, the dynamics  
 175 of the transient sensitivity at 0V may provide further information on the mobility and the concentration  
 176 of mobile ionic species in the material. This will be discussed in a future work. In the present work, we  
 177 will focus on the sensitivity at 0V measured immediately after removing the bias, and develop a model  
 178 that accords accurately the above-mentioned results.

179



180  
 181 Fig. 3. (a) Sensitivity-time measurements for different biasing duration at +10V (b) Sensitivity measured  
 182 immediately after removing the bias for different previously applied bias. The biasing duration is 400  
 183 seconds. Blue dotted line is an eye guideline.

## 184 4. Model

185

186 In the following, we propose to model the sensitivity of a 2-mm thick MAPbBr<sub>3</sub> planar device  
 187 considering the following assumptions : (i) the electric field is mainly uniform throughout the device;  
 188 (ii) an internal electric field is created upon biasing, and is equivalent to the residual electric field at 0V  
 189 immediately after removing the bias ; (iii) the internal electric field opposes the externally applied  
 190 electric field (see Fig.3a). Regarding (i), the simulations carried out by Alvarez *et al.* show that the  
 191 accumulation of mobile ions forms a depletion region at the very vicinity of the electrodes, with a  
 192 depletion width only up to a few micrometers when the device is previously biased at 10V.[19] Besides,  
 193 the electric field as function of the depth is mostly flat in the bulk,[19], [26] and for a 2-mm thick device  
 194  $w_i \ll L$ , thus the internal field in the bulk region is approximated by  $\frac{V_i}{L}$  (Fig. 4). We can consider a uniform  
 195 electric field in the sensitivity model provided that the penetration depth of the X-rays is much greater  
 196 than the depletion width. In the present case, the hard RQA5 X-rays with a high mean energy of 53 keV  
 197 generate charges throughout the volume of the 2-mm thick MAPbBr<sub>3</sub> device, as evidenced in Fig.4c  
 198 (dotted line). In addition, we limit our model to rather moderate applied bias (10V), for which the  
 199 electric field distortion is limited. Finally, the assumptions (ii) and (iii) are justified by the dark current  
 200 and sensitivity-time measurements displayed in Fig.2 and Fig.3.

201 Due to high penetration depth of the X-rays used in the present study, using the two-carriers Hecht  
 202 equation (3) is compulsory. Considering the assumptions listed above, the model reads as follow. The  
 203 sensitivity under bias measured a fraction of time before removing the bias writes:

$$204 \quad S(V - Vi) = \int s_0(x) \eta_{bias}(x, V - Vi) dx \quad (5)$$

$$205 \quad \eta_{bias}(x, V - Vi) = \frac{\mu_e \tau_e (V - Vi)}{L^2} \left[ 1 - e^{-\frac{L(L-x)}{\mu_e \tau_e (V - Vi)}} \right] + \frac{\mu_h \tau_h V}{L^2} \left[ 1 - e^{-\frac{xL}{\mu_h \tau_h (V - Vi)}} \right] \quad (6)$$

206 The sensitivity at 0V measured immediately after removing the bias writes :

$$207 \quad S(Vi) = \int s_0(x) \eta_{short}(x, Vi) dx \quad (7)$$

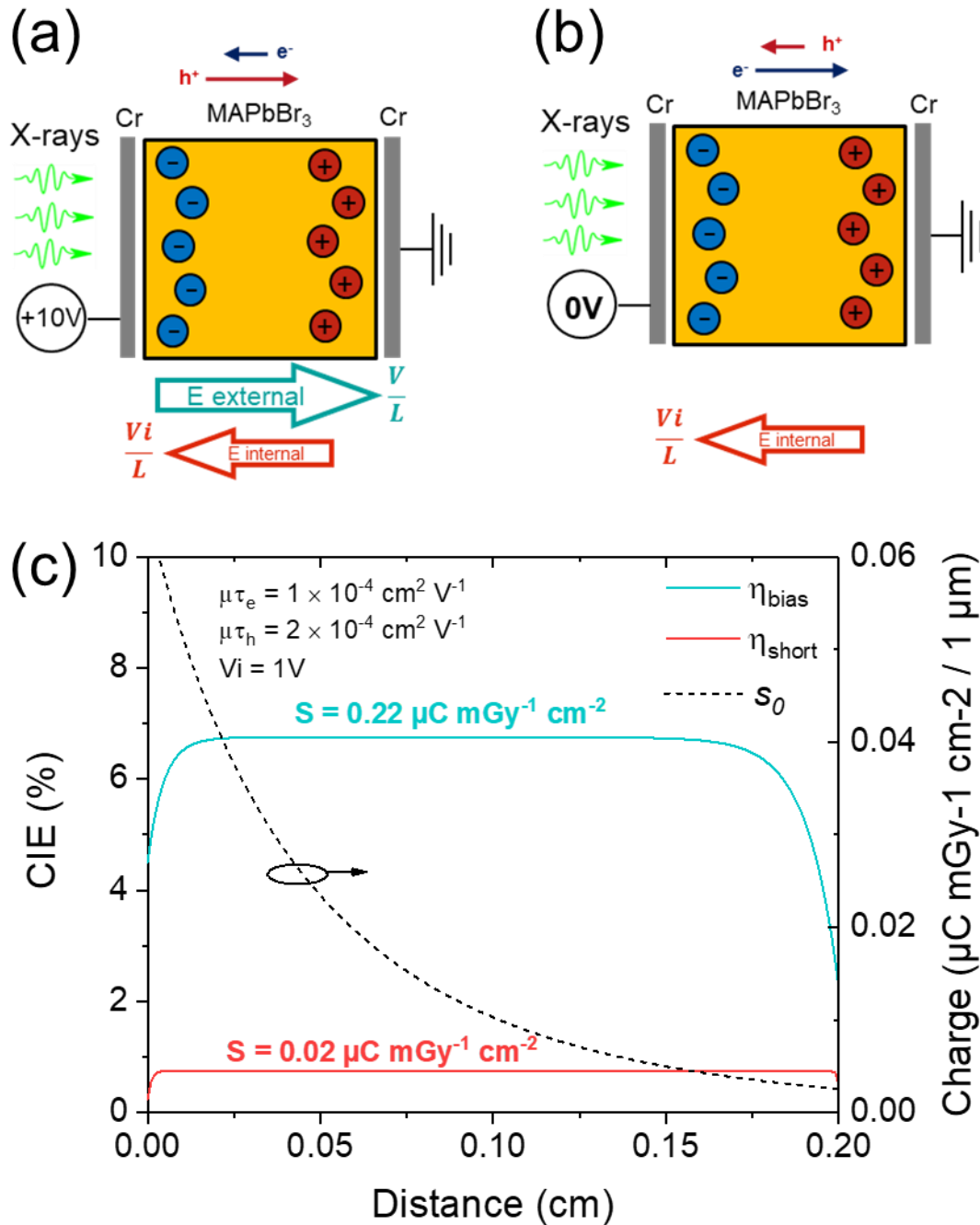
208

$$209 \quad \eta_{short}(x, Vi) = \frac{\mu_e \tau_e Vi}{L^2} \left[ 1 - e^{-\frac{xL}{\mu_e \tau_e Vi}} \right] + \frac{\mu_h \tau_h Vi}{L^2} \left[ 1 - e^{-\frac{L(L-x)}{\mu_h \tau_h Vi}} \right] \quad (8)$$

210

211 Where  $V$  is the externally applied bias,  $Vi$  is the potential associated to the internal electric field  $= \frac{Vi}{L}$ ,  
 212  $\eta_{bias}$  is the CIE before removing the bias and  $\eta_{short}$  is the CIE after removing the bias and  $x$  is the  
 213 position of interaction of the X-ray in the MAPbBr<sub>3</sub> device. Note that the equations (6) and (8)  
 214 correspond to the case where a positive bias is applied to the irradiated electrode. For a 2-mm thick  
 215 MAPbBr<sub>3</sub> device and borderline hard ~50 keV X-rays, the response in biasing conditions is slightly  
 216 dominated by hole transport (Fig.4a), and the response in short-circuit conditions is slightly dominated  
 217 by electron transport (Fig.4b). Fig. 4c displays the results of the model calculation for the following  
 218 input parameters :  $\mu_e \tau_e = 1.10^{-4} \text{ cm}^2 \text{ V}^{-1}$ ;  $\mu_h \tau_h = 2.10^{-4} \text{ cm}^2 \text{ V}^{-1}$ ;  $L = 0.2 \text{ cm}$ ;  $V = 10\text{V}$ ;  $Vi = 1\text{V}$ . It can be  
 219 seen that the total induced charge under X-rays – or in other word, the sensitivity  $S$  – is close to the  
 220 experimental value shown in Fig.3a ( $S \approx 0.2 \text{ } \mu\text{C mGy}^{-1} \text{ cm}^{-2}$  at 10V and  $S \approx 0.02 \text{ } \mu\text{C mGy}^{-1} \text{ cm}^{-2}$  at 0V).  
 221 Notably, it implies that the internal electrical field at 10V could be as high as 5 V/cm; which  
 222 corresponds to 10 percent of the externally applied electric field (50 V/cm). It indicates that there could  
 223 be a 10% uncertainty on the value of the applied bias that could partially explain the discrepancy  
 224 between the  $S$ - $V$  plot and the Hecht model, as depicted in Fig.1b.

225



226  
227  
228  
229  
230  
231

Fig. 4. Schematics of the device during (a) the biasing condition and (b) the short-circuit condition. The internal and external electric fields are deemed uniform throughout the device (c) Results of the calculation. Blue and red lines are the CIE as function of distance at 10V and 0V respectively. Black dotted line is the photogenerated charge. The x-axis is the distance in the device from the irradiated electrode ( $x=0$ ) to the back electrode ( $x=L=2\text{mm}$ ). Calculated for RQA5 X-rays.

232

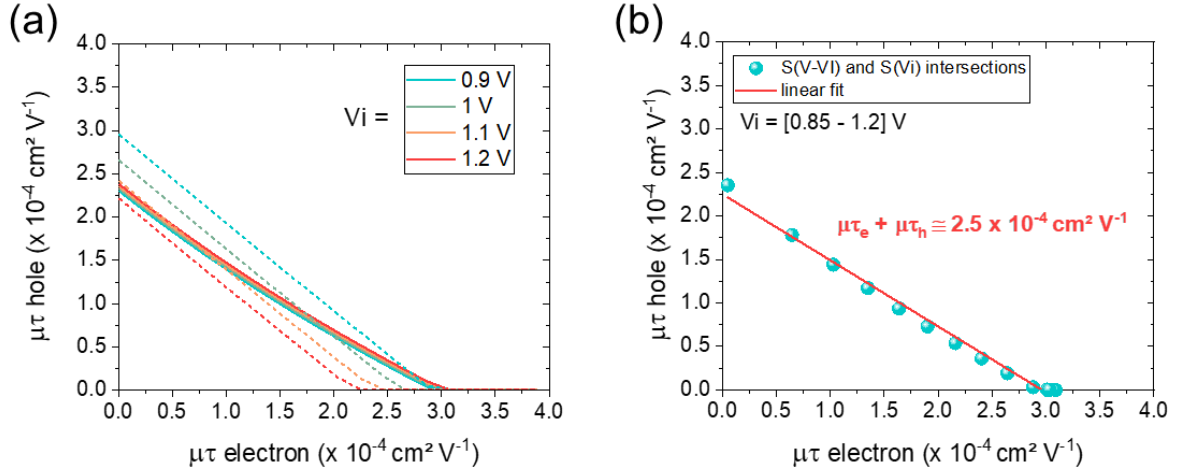
## 5. Results and discussion

233  
234

235 In this part, it will be demonstrated how the model allows to estimate precisely the internal electric  
236 field in a Cr/MAPbBr<sub>3</sub>/Cr planar device, as well as reasonable ranges for the  $\mu_e\tau_e$  and  $\mu_h\tau_h$  products.

237 The set of equation (5-8) has 3 unknown parameters :  $\mu_e\tau_e$  ;  $\mu_h\tau_h$  and  $V_i$ . Only two experimental  
 238 measurement of sensitivity are used as inputs for the model :  $S$  at 10V before removing the bias, and  
 239  $S$  at 0V immediately after removing the bias. Hence it may provide only a set of solution ( $\mu_e\tau_e$ ,  
 240  $\mu_h\tau_h, V_i$ ). Nonetheless, we will see that the set of possible solution is limited and allow to establish a  
 241 credible range for the above cited parameters.

242 The model was applied to the measurements displayed in Fig.3a for a MAPbBr<sub>3</sub> single crystal planar  
 243 device with 2-mm thickness, 5 x 5 mm<sup>2</sup> chromium electrodes and RQA5 X-rays. The picture of the  
 244 device is shown in Fig. 2a. Further details on the fabrication of the device and the experimental setup  
 245 are supplied in the Methods section. The experimental measurement of sensitivity gives :  $S(10-V_i) =$   
 246  $0.17 \mu\text{C mGy}^{-1} \text{cm}^{-2}$  and  $S(V_i) = 0.021 \mu\text{C mGy}^{-1} \text{cm}^{-2}$ . We calculated all the possible ( $\mu_e\tau_e, \mu_h\tau_h, V_i$ ) for  
 247 which  $S(10-V_i)$  and  $S(V_i)$  are both equal to the above cited values at the same time. The Fig.5a. displays  
 248 the results of the calculation in the ( $\mu_e\tau_e, \mu_h\tau_h$ ) space. For all  $V_i$ ,  $S(10-V_i)$  and  $S(V_i)$  form two straight  
 249 lines that only cross for a limited number of  $V_i$  values ranging from 0.9 V to 1.2 V. The intersection of  
 250 the two  $S(10-V_i)$  and  $S(V_i)$  lines implies that it exists a set of ( $\mu_e\tau_e, \mu_h\tau_h, V_i$ ) that allows to fully describe  
 251 the experimental sensitivity measured under X-ray, or in other word, it provides a solution of the  
 252 equation system. Hence, all the possible solutions (intersections) for this experiment are displayed in  
 253 Fig. 5b. It allows us to establish that the internal electric field  $E_i = \frac{V_i}{L}$  is in the range [4.4 – 5.6] V/cm,  
 254 or is equal to 5.1 V/cm with 15% uncertainty. Regarding the possible values for ( $\mu_e\tau_e, \mu_h\tau_h$ ), the range  
 255 of solutions is much broader.  $\mu_e\tau_e$  spans from  $5 \times 10^{-6} \text{cm}^2 \text{V}^{-1}$  to  $3 \times 10^{-4} \text{cm}^2 \text{V}^{-1}$  and  $\mu_h\tau_h$  spans from  
 256  $1 \times 10^{-7} \text{cm}^2 \text{V}^{-1}$  to  $2.5 \times 10^{-4} \text{cm}^2 \text{V}^{-1}$ . The uncertainty on the individual  $\mu_e\tau_e$  and  $\mu_h\tau_h$  values is therefore  
 257 very high with this model. Nonetheless, more notable is the fact that this experiment computes quite  
 258 precisely a value for the sum  $\mu_e\tau_e + \mu_h\tau_h$ , as displayed by the linear fit in Fig. 5b. All of these solutions  
 259 are aligned, and the sum  $\mu_e\tau_e + \mu_h\tau_h$  has a near constant value of  $\sim 2.5 \times 10^{-4} \text{cm}^2 \text{V}^{-1}$ . Here, the range  
 260 of solutions is a straight line because we are dealing with small electric fields, which means that the  
 261 mean free path of the charge carriers is small compared to the thickness of the device. In that peculiar  
 262 case, the exponential term in the Hecht equation becomes negligible, and the CIE becomes  $\simeq \frac{\mu_e\tau_e V}{L^2} +$   
 263  $\frac{\mu_h\tau_h V}{L^2} = \frac{(\mu_e\tau_e + \mu_h\tau_h)V}{L^2}$ . Substituting this into equation 7 gives  $2.6 \times 10^{-4} \text{cm}^2 \text{V}^{-1}$  for  $V_i = 1\text{V}$ , which is  
 264 consistent with the above results. The information on the sum  $\mu_e\tau_e + \mu_h\tau_h$  provides new insights into  
 265 the charge transport properties of the material. Using other complementary measurements, it is then  
 266 possible to fully rationalize the transport of the material. For instance, the rather symmetric S-V plot  
 267 displayed in Fig.1. indicate that the respective  $\mu_e\tau_e$  and  $\mu_h\tau_h$  values probably have the same order of  
 268 magnitude. Otherwise, the S-V data would be very asymmetrical for the X-ray exposure conditions and  
 269 device thickness used in this work. (see supplementary Fig.S6). This is consistent with photocurrent  
 270 measurements made under the AM-241 source, which indicate that the  $\mu_e\tau_e$  and  $\mu_h\tau_h$  could be  
 271 separated only by a factor of 2.[34], [35]



272

273

274

275

276

277

Fig.5. Calculations of the  $(\mu_e\tau_e, \mu_h\tau_h, V_i)$  solutions for  $S(10-V_i) = 0.17 \mu\text{C mGy}^{-1} \text{ cm}^{-2}$  (solid lines) and  $S(V_i) = 0.021 \mu\text{C mGy}^{-1} \text{ cm}^{-2}$  (dash lines). (a)  $S(10-V)$  and  $S(V)$  lines as function of  $V_i$ . Each color corresponds to a different  $V_i$  input value. (b) Intersections of the  $S(10-V)$  and  $S(V)$  lines with  $V_i$  varying from 0.85 to 1.2V.

278

279

280

281

282

283

284

285

286

287

288

289

290

291

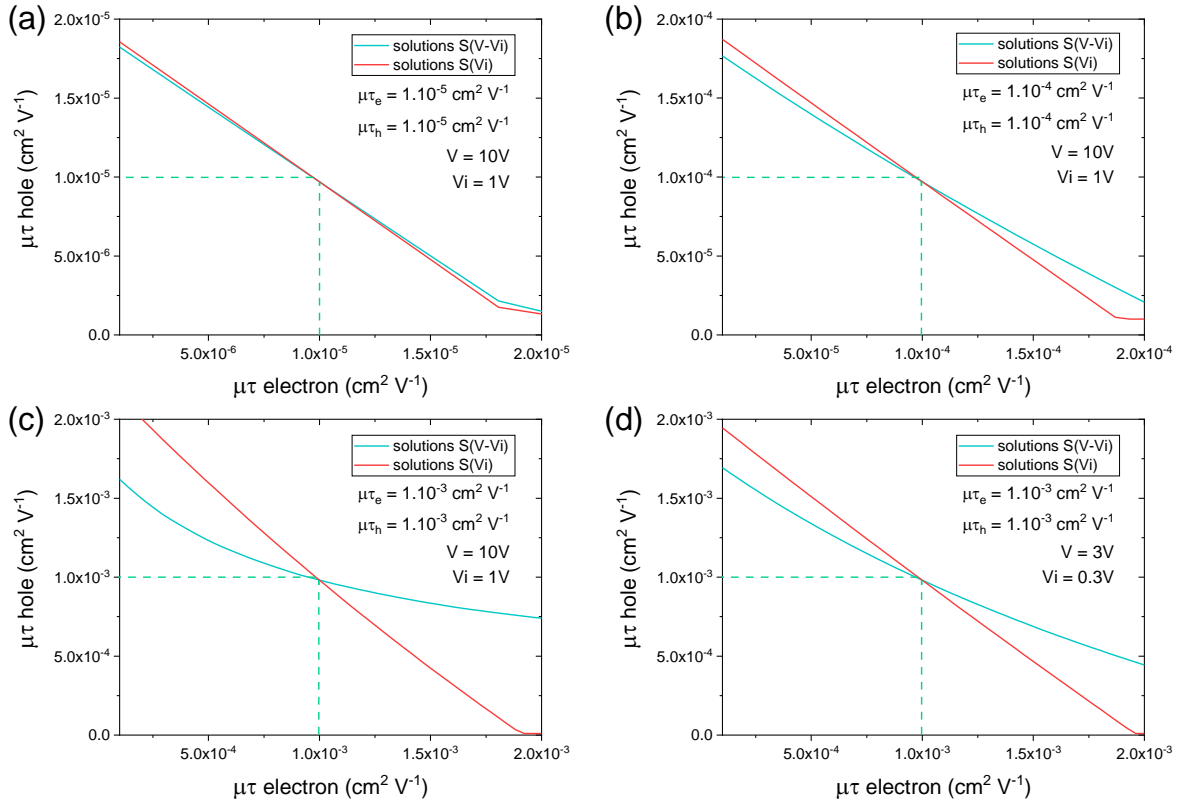
292

293

294

295

To assess the robustness of the method, we simulated the response of MAPbBr<sub>3</sub> devices for hypothetical  $(\mu_e\tau_e, \mu_h\tau_h, V_i)$  and thickness values. Several of these simulations are displayed in Fig.6. Remarkably, we noticed that it does not seem to exist a case where the two  $S(10-V_i)$  and  $S(V_i)$  lines doesn't cross in one point in the  $(\mu_e\tau_e, \mu_h\tau_h)$  space for a single  $V_i$  value. As seen in Fig. 6a and 6b, the lines are almost parallel when the  $(\mu_e\tau_e, \mu_h\tau_h)$  values are moderate ( $\leq 1 \times 10^{-4} \text{ cm}^2 \text{ V}^{-1}$ ). When the charge transport is better ( $\approx 1 \times 10^{-3} \text{ cm}^2 \text{ V}^{-1}$ ) as in Fig 6c, the model still provides a single solution for a single  $V_i$  value. In the latter case however, the  $S(V-V_i)$  line is no longer parallel to the  $S(V_i)$  line. It implies that the error on  $V_i$  is much higher than in the moderate charge transport case since the position of the  $S(V_i)$  line varies sizably with the  $V_i$  value (Fig. 6a-b). It can be understood by considering that high sensitivity increases the total number of possible solutions for the model. If the transport is high, the sensitivity is high accordingly, and the model struggles to resolve accurately a value for  $V_i$ . If such a case were to be met, a quick fix would consist of reducing the applied bias  $V$  in order to reduce the charge carrier mean free path. As seen in Fig. 6d, it results in a reduction of the curvature of the  $S(V-V_i)$ , and an increased precision on the estimation of  $V_i$ . In addition, having straight  $S(V-V_i)$  and  $S(V_i)$  lines is associated to a low mean free path for the charge carriers, which allows to establish accurately a value of the sum  $\mu_e\tau_e + \mu_h\tau_h$  (see Fig. 5b). Lowering the bias during the biasing step to reduce the mean free path is thus interesting to increase the precision for both the internal potential  $V_i$ , and the sum of the mobility lifetime products  $\mu_e\tau_e + \mu_h\tau_h$ .



296  
 297 Fig. 6. Calculation of the  $S(V-V_i)$  and  $S(V_i)$  lines for different  $(\mu_e \tau_e, \mu_h \tau_h, V_i)$  input values. The thickness  
 298 of the device is 2 mm. The intersection of the  $S(V-V_i)$  and  $S(V_i)$  lines provides the solution of the  
 299 equation system.

300 Finally, we can use this model to estimate an order of magnitude for the space-charge density  
 301 generated upon biasing. First, we considered the parallel plate capacitor approximation which reads  
 302  $Q = C \times V$  and  $Q = \frac{\epsilon \epsilon_0 S}{L}$  with  $Q$  the charge,  $C$  the capacity,  $\epsilon$  the relative permittivity of the  
 303 perovskite,  $\epsilon_0$  the vacuum permittivity,  $S$  the electrode surface area and  $L$  the device thickness. From  
 304 the Fig.5, we can assume a value for  $V_i \approx 1V$ , corresponding to a charge of 50 nC. If we assume that this  
 305 charge was extracted from the bulk of the crystals, e.g. via migration of charged ionic species, and that  
 306 the totality of the charges reached the electrode, we can establish that the charge density in the bulk  
 307 was initially  $1 \mu C cm^{-3}$ . Now if we consider that this charge originate from moving ionic species, it would  
 308 represent a density of  $10^{+13}$  ions  $cm^{-3}$ , which is in accordance with ionic concentrations previously  
 309 measured in similar MAPbBr<sub>3</sub> single crystal devices.[19], [36]

310

## 311 6. Conclusion

312

313 In this paper, we provide robust experimental evidences for the presence of an internal electric field  
 314 in Cr/MAPbBr<sub>3</sub>/Cr X-ray detectors that builds up upon biasing. This internal electric field generates a  
 315 significant but decaying response under X-rays at 0V; and diminish the net electric field in the device  
 316 under bias. We propose that the discordance between the experimental  $S-V$  plots and the Hecht model  
 317 is due to the internal electric field that alters the  $S-V$  relationship. Starting from a modified version of  
 318 the Hecht equation, we developed a model for the sensitivity that involves an internal electric field  
 319 with opposed sign to the externally applied electric field. We found that the model can accurately

320 predict a value for the internal electric field, even without prior information about the charge transport  
321 properties of the material. Notably, the actual internal electric field in the bulk of our 2-mm MAPbBr<sub>3</sub>  
322 device could be overestimated by about 10% at 50V/cm. In addition, we exploit our model as an  
323 alternative pathway for the evaluation of the  $\mu_e\tau_e$  and  $\mu_h\tau_h$  products, and more precisely for the sum  
324  $\mu_e\tau_e + \mu_h\tau_h$ . We believe that our model rationalize some intriguing electrical properties of MAPbBr<sub>3</sub>  
325 detectors under bias such as dark current relaxation and zero-bias sensitivity; and could be extended  
326 to other perovskite composition exhibiting dark current relaxation at zero-bias such as CH<sub>3</sub>NH<sub>3</sub>PbI<sub>3</sub> and  
327 CsPbBr<sub>3</sub>. [32], [37] Future work will bring further information on the remnant charge density in the  
328 MAPbBr<sub>3</sub> material by exploiting the dynamics of sensitivity decay at zero-bias.

329

## 330 **Methods**

331

### 332 **Device Fabrication**

333 Millimeter-sized methylammonium lead tribromide (MAPbBr<sub>3</sub>) single crystals were grown using the  
334 Modified Inverse Temperature Crystallization (MITC) method described in details in previous  
335 works.[9], [16], [19] Briefly, the precursor solutions were prepared in an argon-filled glovebox by  
336 dissolving PbBr<sub>2</sub> (ultra dry, 99.999 % metal basis) and MABr ( $\geq 99\%$ ) in anhydrous N,N-  
337 Dimethylformamide with 1:1 molar ratio. The growth was carried out using a crystal seed, as described  
338 in [9]. Both the large facets of the crystals were mechanically polished with SiC disks and isopropanol,  
339 then with fabric disks and diamond paste in order to obtain a mirror grade quality. 100-nm Cr  
340 electrodes were subsequently thermally evaporated on both facets. We found that proper polishing  
341 and chromium electrodes enhance the electrical stability of the devices under bias, as also noted in  
342 previous works.[15], [38]

### 343 **X-ray characterization**

344 Dark current and sensitivity measurements were conducted on the same setup using a Keithley 428  
345 current amplifier and a Keithley 487 power supply. The samples were irradiated with short X-ray pulses  
346 (4 Hz repetition rate, 100 ms duration) using a medical-grade pulsed X-ray tube with tungsten anode  
347 and 70 kVp accelerating voltage. The incident X-rays were filtrated through a 0.8 mm beryllium window  
348 and 23.5 mm additionnal aluminium filters to yield a RQA5 spectrum, following the IEC 62220  
349 International Standard. The incident dose was calibrated with a PTW Unidos dosimeter, yielding  $24 \pm$   
350  $0.6 \mu\text{Gy}_{\text{air}}$  per pulse. The X-rays were collimated through a  $12.6 \text{ mm}^2$  hole pierced in a  $\approx 5\text{mm}$ -thick lead  
351 plate. Due to long-range diffusion of the X-ray generated charge carriers in the area not covered by  
352 the electrodes, the collimation is necessary to properly evaluate the absorption surface area of the  
353 incident X-rays, hence the sensitivity. Each sensitivity measurement consisted of 10 X-ray pulses that  
354 were averaged to reduce experimental error (see Fig. S7). Typical uncertainty on the sensitivity  
355 measurement was 3%.

### 356 **Numerical simulation**

357 The elemental charge deposited in the MAPbBr<sub>3</sub> material  $s_0$  and the maximum theoretical sensitivity  
358  $S_0$  were calculated using Eq. 9 and Eq. 10 that read:

$$359 \quad S_0(x) = \frac{e \times E^*(x)}{W_{\pm}} \quad (9)$$

360 
$$E^*(x) = \int N(E) \times E \times A(x, E) dE \quad (10)$$

361 Where  $e$  is the elemental charge ;  $E^*$  is the energy deposited by the X-rays in the perovskite material  
362 (Fig. S8),  $W_{\pm}$  is the electron-hole pair creation energy that was calculated using Klein's rule  $W_{\pm} =$   
363  $\frac{14}{5}E_g + 0.5$  with  $E_g = 2.3$  eV [16], [21] ;  $D$  is the dose per surface area ;  $N$  is the number of incident  
364 photon emitted by the X-ray tube as function of photon energy  $E$ ;  $A$  is the absorbed fraction as function  
365 of the position of interaction of the X-rays in the MAPbBr<sub>3</sub> device. The latter is computed as for Eq. 11  
366 :

367 
$$A(x, E) = T(x, E) - T(x + dx, E) = e^{-\sigma(E)\rho x} - e^{-\sigma(E)\rho(x+dx)} \quad (11)$$

368

369 Where  $T$  is the transmitted fraction;  $\sigma$  is the photon cross section;  $\rho$  is the density (3.8 g cm<sup>-3</sup> for  
370 MAPbBr<sub>3</sub>)[39]. The photon cross section was obtained from NIST photon cross sections database  
371 considering only the photoelectric interaction, assuming that it is the predominant interaction  
372 mechanism in the 20-70 keV energy range for MAPbBr<sub>3</sub>. [40] The number of incident photons  $N$  was  
373 computed for a RQA5 spectrum using the SpekCalc software. [41]–[43] It is given as function of incident  
374 X-ray dose in mGy<sub>air</sub> and per unit area (Fig. S9).

## 375 **Supplementary Material**

376 The Supplementary Material is available free of charge at:

377 Additionnal Hecht equation fitting plots, computations of the energy deposited by the X-rays and the  
378 number of incident photons, examples of X-ray-induced photocurrent pulses under bias and at short-  
379 circuit.

380

## 381 **Author Declaration section**

382

## 383 **Conflict of Interest Statement**

384 The authors have no conflicts to disclose.

## 385 **Author Contributions**

386 F.L.: conceptualization, X-ray characterizations, computations, writing-original draft ; J.M-G. and S.L.:  
387 crystal growth, device fabrication ; J.Z. and J-M.V.: investigations, writing-review and editing , project  
388 administration ; E.G.-D.: conceptualization, methodology, writing-review and editing.

## 389 **Data Availability Statement**

390 The data that support the findings of this study are available from the corresponding authors upon  
391 reasonable request.

## 392 **Acknowledgement**

393 This work has received funding from the European Union's Horizon 2020 research and innovation  
394 program under the Photonics Public-Private Partnership ([www.photonics21.org](http://www.photonics21.org)) with the project  
395 PEROXIS under grant agreement N° 871336.

397 **References**

398

- 399 [1] H. Wei *et al.*, « Sensitive X-ray detectors made of methylammonium lead tribromide perovskite  
400 single crystals », *Nature Photon*, vol. 10, n° 5, p. 333-339, mai 2016, doi:  
401 10.1038/nphoton.2016.41.
- 402 [2] W. Wei *et al.*, « Monolithic integration of hybrid perovskite single crystals with heterogenous  
403 substrate for highly sensitive X-ray imaging », *Nature Photon*, vol. 11, n° 5, p. 315-321, mai 2017,  
404 doi: 10.1038/nphoton.2017.43.
- 405 [3] X. Wang *et al.*, « PIN Diodes Array Made of Perovskite Single Crystal for X-Ray Imaging »,  
406 *physica status solidi (RRL) – Rapid Research Letters*, vol. 12, n° 10, p. 1800380, oct. 2018, doi:  
407 10.1002/pssr.201800380.
- 408 [4] Q. Xu *et al.*, « High-Performance Surface Barrier X-ray Detector Based on Methylammonium  
409 Lead Tribromide Single Crystals », *ACS Appl. Mater. Interfaces*, vol. 11, n° 10, p. 9679-9684,  
410 mars 2019, doi: 10.1021/acsami.8b21605.
- 411 [5] L. Li *et al.*, « Enhanced X-ray Sensitivity of MAPbBr<sub>3</sub> Detector by Tailoring the Interface-States  
412 Density », *ACS Appl. Mater. Interfaces*, vol. 11, n° 7, p. 7522-7528, févr. 2019, doi:  
413 10.1021/acsami.8b18598.
- 414 [6] X. Geng *et al.*, « High-Quality Single Crystal Perovskite for Highly Sensitive X-Ray Detector »,  
415 *IEEE Electron Device Lett.*, vol. 41, n° 2, p. 256-259, févr. 2020, doi:  
416 10.1109/LED.2019.2960384.
- 417 [7] W. Zhang, H. Wang, H. Dong, F. Li, Z. Wang, et Y. Shao, « Mechanical polishing with chemical  
418 passivation of perovskite single crystals for high-performance X-ray detectors », *J. Mater. Chem.*  
419 *C*, vol. 10, n° 45, p. 17353-17363, 2022, doi: 10.1039/D2TC03850A.
- 420 [8] M. I. Saidaminov *et al.*, « High-quality bulk hybrid perovskite single crystals within minutes by  
421 inverse temperature crystallization », *Nat Commun*, vol. 6, n° 1, p. 7586, nov. 2015, doi:  
422 10.1038/ncomms8586.
- 423 [9] S. Amari, J.-M. Verilhac, E. Gros D'Aillon, A. Ibanez, et J. Zaccaro, « Optimization of the  
424 Growth Conditions for High Quality CH<sub>3</sub>NH<sub>3</sub>PbBr<sub>3</sub> Hybrid Perovskite Single Crystals »,  
425 *Crystal Growth & Design*, vol. 20, n° 3, p. 1665-1672, mars 2020, doi: 10.1021/acs.cgd.9b01429.
- 426 [10] F. Yao *et al.*, « Room-temperature liquid diffused separation induced crystallization for high-  
427 quality perovskite single crystals », *Nat Commun*, vol. 11, n° 1, p. 1194, mars 2020, doi:  
428 10.1038/s41467-020-15037-x.
- 429 [11] K. Hecht, « Zum Mechanismus des lichtelektrischen Primärstromes in isolierenden Kristallen »,  
430 *Z. Physik*, vol. 77, n° 3-4, p. 235-245, mars 1932, doi: 10.1007/BF01338917.
- 431 [12] T. E. Schlesinger et R. B. James, *Semiconductors for Room Temperature Nuclear Detector*  
432 *Applications*, Academic Press., vol. 43. in *Semiconductors and Semimetals*, vol. 43. 1995.
- 433 [13] G. Bertolini et A. Coche, *Semiconductor Detectors*, Eds. Interscience. Wiley, 1968.
- 434 [14] J. Song *et al.*, « Facile Strategy for Facet Competition Management to Improve the Performance  
435 of Perovskite Single-Crystal X-ray Detectors », *J. Phys. Chem. Lett.*, vol. 11, n° 9, p. 3529-3535,  
436 mai 2020, doi: 10.1021/acs.jpcclett.0c00770.
- 437 [15] R. Tan *et al.*, « Characterization of solution grown 3D polycrystalline methylammonium lead  
438 tribromide for x-ray detection », *Journal of Applied Physics*, vol. 132, n° 20, p. 204503, nov.  
439 2022, doi: 10.1063/5.0100362.
- 440 [16] J. M. Guillén *et al.*, « MAPb(Br<sub>1-x</sub>Cl<sub>x</sub>)<sub>3</sub> Hybrid Perovskite Materials for Direct X-ray  
441 Detection », mars 2023, doi: <https://doi.org/10.1021/acsaelm.3c00114>.
- 442 [17] Z. Gou *et al.*, « Self-Powered X-Ray Detector Based on All-Inorganic Perovskite Thick Film with  
443 High Sensitivity Under Low Dose Rate », *Phys. Status Solidi RRL*, vol. 13, n° 8, p. 1900094, août  
444 2019, doi: 10.1002/pssr.201900094.
- 445 [18] K. Sakhatskyi *et al.*, « Stable perovskite single-crystal X-ray imaging detectors with single-photon  
446 sensitivity », *Nat. Photon.*, mai 2023, doi: 10.1038/s41566-023-01207-y.

- 447 [19] A. O. Alvarez *et al.*, « Ionic Field Screening in MAPbBr<sub>3</sub> Crystals Revealed from Remnant  
448 Sensitivity in X-ray Detection », *ACS Phys. Chem Au*, p. acsphyschemau.3c00002, mai 2023, doi:  
449 10.1021/acsphyschemau.3c00002.
- 450 [20] S. Ramo, « Currents Induced by Electron Motion », *Proc. IRE*, vol. 27, n° 9, p. 584-585, sept.  
451 1939, doi: 10.1109/JRPROC.1939.228757.
- 452 [21] C. A. Klein, « Bandgap Dependence and Related Features of Radiation Ionization Energies in  
453 Semiconductors », *Journal of Applied Physics*, vol. 39, n° 4, p. 2029-2038, mars 1968, doi:  
454 10.1063/1.1656484.
- 455 [22] Y. He *et al.*, « High spectral resolution of gamma-rays at room temperature by perovskite  
456 CsPbBr<sub>3</sub> single crystals », *Nat Commun*, vol. 9, n° 1, p. 1609, déc. 2018, doi: 10.1038/s41467-  
457 018-04073-3.
- 458 [23] M. Zanichelli, A. Santi, M. Pavesi, et A. Zappettini, « Charge collection in semi-insulator  
459 radiation detectors in the presence of a linear decreasing electric field », *J. Phys. D: Appl. Phys.*,  
460 vol. 46, n° 36, p. 365103, sept. 2013, doi: 10.1088/0022-3727/46/36/365103.
- 461 [24] F. Principato, A. A. Turturici, M. Gallo, et L. Abbene, « Polarization phenomena in Al/p-CdTe/Pt  
462 X-ray detectors », *Nuclear Instruments and Methods in Physics Research Section A: Accelerators,  
463 Spectrometers, Detectors and Associated Equipment*, vol. 730, p. 141-145, déc. 2013, doi:  
464 10.1016/j.nima.2013.05.157.
- 465 [25] H. Meng *et al.*, « Simulation of the Charge Collection in a Nonuniform Electric Field for MAPbI<sub>3</sub>  
466 Semiconductor Nuclear Detector With Schottky Contact », *IEEE Trans. Nucl. Sci.*, vol. 69, n° 9,  
467 p. 1990-1998, sept. 2022, doi: 10.1109/TNS.2022.3194317.
- 468 [26] S. Jia *et al.*, « Ion-Accumulation-Induced Charge Tunneling for High Gain Factor in P-I-N-  
469 Structured Perovskite CH<sub>3</sub>NH<sub>3</sub>PbI<sub>3</sub> X-Ray Detector », *Adv. Mater. Technol.*, p. 2100908, déc.  
470 2021, doi: 10.1002/admt.202100908.
- 471 [27] O. Baussens *et al.*, « An insight into the charge carriers transport properties and electric field  
472 distribution of CH<sub>3</sub>NH<sub>3</sub>PbBr<sub>3</sub> thick single crystals », *Appl. Phys. Lett.*, vol. 117, n° 4, p.  
473 041904, juill. 2020, doi: 10.1063/5.0011713.
- 474 [28] Y. Luo *et al.*, « Direct Observation of Halide Migration and its Effect on the Photoluminescence  
475 of Methylammonium Lead Bromide Perovskite Single Crystals », *Adv. Mater.*, vol. 29, n° 43, p.  
476 1703451, nov. 2017, doi: 10.1002/adma.201703451.
- 477 [29] J. Pospisil *et al.*, « Reversible Formation of Gold Halides in Single-Crystal Hybrid-Perovskite/Au  
478 Interface upon Biasing and Effect on Electronic Carrier Injection », *Adv. Funct. Mater.*, vol. 29, n°  
479 32, p. 1900881, août 2019, doi: 10.1002/adfm.201900881.
- 480 [30] M. García-Batlle *et al.*, « Moving Ions Vary Electronic Conductivity in Lead Bromide Perovskite  
481 Single Crystals through Dynamic Doping », *Adv. Electron. Mater.*, vol. 6, n° 10, p. 2000485, oct.  
482 2020, doi: 10.1002/aelm.202000485.
- 483 [31] M. García-Batlle *et al.*, « Coupling between Ion Drift and Kinetics of Electronic Current  
484 Transients in MAPbBr<sub>3</sub> Single Crystals », *ACS Energy Lett.*, vol. 7, n° 3, p. 946-951, mars 2022,  
485 doi: 10.1021/acsenerylett.1c02578.
- 486 [32] M. García-Batlle *et al.*, « Mobile Ion-Driven Modulation of Electronic Conductivity Explains  
487 Long-Timescale Electrical Response in Lead Iodide Perovskite Thick Pellets », *ACS Appl. Mater.  
488 Interfaces*, vol. 13, n° 30, p. 35617-35624, août 2021, doi: 10.1021/acsaami.1c06046.
- 489 [33] O. Almora, D. Miravel, G. Ilario, et G.-B. Germà, « Long-Term Field Screening by Mobile Ions  
490 in Thick Metal Halide Perovskites: Understanding Saturation Currents », *physica status solidi  
491 (RRL) – Rapid Research Letters*, n° 16, p. 2200336, 2022, doi: DOI: 10.1002/pssr.202200336.
- 492 [34] S. H. Bennett *et al.*, « Charge transport comparison of FA, MA and Cs lead halide perovskite  
493 single crystals for radiation detection », *Front. Detect. Sci. Technol.*, vol. 1, p. 1249892, sept.  
494 2023, doi: 10.3389/fdest.2023.1249892.
- 495 [35] X. Liu, H. Zhang, B. Zhang, J. Dong, W. Jie, et Y. Xu, « Charge Transport Behavior in Solution-  
496 Grown Methylammonium Lead Tribromide Perovskite Single Crystal Using  $\alpha$  Particles », *J. Phys.  
497 Chem. C*, vol. 122, n° 26, p. 14355-14361, juill. 2018, doi: 10.1021/acs.jpcc.8b03512.
- 498 [36] E. A. Duijnste, V. M. Le Corre, M. B. Johnston, L. J. A. Koster, J. Lim, et H. J. Snaith,  
499 « Understanding Dark Current-Voltage Characteristics in Metal-Halide Perovskite Single  
500 Crystals », *Phys. Rev. Applied*, vol. 15, n° 1, p. 014006, janv. 2021, doi:  
501 10.1103/PhysRevApplied.15.014006.

- 502 [37]B.-B. Zhang *et al.*, « Defect proliferation in CsPbBr<sub>3</sub> crystal induced by ion migration », *Appl.*  
503 *Phys. Lett.*, vol. 116, n° 6, p. 063505, févr. 2020, doi: 10.1063/1.5134108.
- 504 [38]R. Tan, B. Dryzhakov, J. Charest, B. Hu, M. Ahmadi, et E. Lukosi, « Improved Radiation Sensing  
505 with Methylammonium Lead Tribromide Perovskite Semiconductors », *Nuclear Instruments and*  
506 *Methods in Physics Research Section A: Accelerators, Spectrometers, Detectors and Associated*  
507 *Equipment*, vol. 986, p. 164710, janv. 2021, doi: 10.1016/j.nima.2020.164710.
- 508 [39]D. Weber, « CH<sub>3</sub>NH<sub>3</sub>PbX<sub>3</sub>, ein Pb(II)-System mit kubischer Perowskitstruktur / CH<sub>3</sub>NH<sub>3</sub>PbX<sub>3</sub>,  
509 a Pb(II)-System with Cubic Perovskite Structure », *Zeitschrift für Naturforschung B*, vol. 33, n°  
510 12, p. 1443-1445, déc. 1978, doi: 10.1515/znb-1978-1214.
- 511 [40]NIST, « XCOM: Photon Cross Sections Database ». [En ligne]. Disponible sur:  
512 <https://physics.nist.gov/PhysRefData/Xcom/html/xcom1.html>
- 513 [41]G. G. Poludniowski et P. M. Evans, « Calculation of x-ray spectra emerging from an x-ray tube.  
514 Part I. Electron penetration characteristics in x-ray targets », *Medical Physics*, vol. 34, n° 6Part1,  
515 p. 2164-2174, juin 2007, doi: 10.1118/1.2734725.
- 516 [42]G. G. Poludniowski, « Calculation of x-ray spectra emerging from an x-ray tube. Part II. X-ray  
517 production and filtration in x-ray targets », *Medical Physics*, vol. 34, n° 6Part1, p. 2175-2186, juin  
518 2007, doi: 10.1118/1.2734726.
- 519 [43]G. Poludniowski, G. Landry, F. DeBlois, P. M. Evans, et F. Verhaegen, « SpekCalc : a program to  
520 calculate photon spectra from tungsten anode x-ray tubes », *Phys. Med. Biol.*, vol. 54, n° 19, p.  
521 N433-N438, oct. 2009, doi: 10.1088/0031-9155/54/19/N01.
- 522